PAPER

Check for updates

Two new inorganic–organic hybrid zinc phosphites and their derived ZnO/ZnS heterostructure for efficient photocatalytic hydrogen production†

Yayong Sun,‡[ab] Fupeng Wang,‡[a] Yunlei Fu,[a] Chao Chen,[a] Xuanyi Wang,[a] Zhenyu Xiao, [iD] *[a] Yanru Liu,[a] Jixiang Xu,[a] Bin Li*[a] and Lei Wang [iD] [a]

Two novel inorganic–organic hybrid zinc phosphites, namely, $[Zn(1,2\text{-bimb})_{0.5}(HPO_3)]_n$ (**1**) and $[Zn(1,4\text{-bmimb})_{0.5}(HPO_3)]_n$ (**2**), (1,2-bimb = 1,2-bis(imidazol-1ylmethyl)benzene; 1,4-bmimb = 1,4-bis((2-methyl-1H-imidazol-1yl)methyl)benzene) were synthesized for the first time by hydrothermal reaction. Compound **1** generates a three-dimensional (3D) pillared-layer structure with a 2-nodal 3,4-connected **3,4T15** topology. While compound **2** exhibits a 2D hybrid zinc phosphite sheet with a 3,4-connected **3,4L83** topology network. Utilizing compound **1** and compound **2** as templates and Na_2S as an etching agent, a series of highly efficient ZnO/ZnS photocatalysts were obtained. The optimized **1-160** sample demonstrates the highest evolution rate of 22.6 mmol g^{-1} h^{-1}, exceeding the rate of commercial ZnS samples by more than 14.5 times. The remarkable photocatalytic activity should be attributed to the unique heterojunction structure which shortens the free path of charge carriers and enhances the charge separation efficiency. This work provides a facile strategy for preparing photocatalysts with efficient photocatalytic hydrogen production derived from inorganic–organic hybrid material.

1. Introduction

Inorganic–organic hybrid materials as a kind of functional porous material are one of the research hotpots in materials chemistry, not only because of their precise and intriguing structures but also for their potential applications in the fields of chemical separation, gas storage, catalysis, and fluorescent materials.[1–6] To date, the employment of different structure-directing or auxiliary N-donor ligands, has been recognized as an efficient strategy to fabricate new inorganic–organic hybrid materials with novel structures.[7–13] Among the N-donor ligands, the bis(imidazole) ligand can adopt subtly different conformations to meet the different geometrical requirements of complexes in the synthesis process (such as metal ions, molar

ratios, pH value, temperature and time, etc.) due to its flexibility.[14–16] For example, the Hanson group reported two different structures that were synthesized by the same ligand (1,3-bis(imidazol-1-ylmethyl)benzene), reaction temperature and time, but with a different ligand-to-zinc ratio.[17] Therefore, the careful selection of N-donor ligands with different lengths, steric effects, conformations and coordination modes as secondary auxiliary ligands is one of the most important factors for the rational design of diverse complexes with specific physical and chemical properties.[18–21] Such as, Wang's group reported a 3D tubular porous structure of an organic-zinc-phosphite through 1,2,4,5-tetrakis(imidazol-1-ylmethyl) benzene, which exhibits high capacity for CO_2 adsorption and interesting optical properties of LED devices.[2] Meanwhile, utilizing 1,3,5-tris(1-imidazolyl)benzene, Wang et al. prepared a serials of inorganic–organic hybrid zinc phosphites framework, which presents excellent phosphorescence property.[13] Very recently, by introducing bis(imidazole) ligand into Zn-phosphate system, we reported two inorganic–organic hybrid zinc phosphate frameworks for photocatalytic hydrogen evolution application.[22]

Photocatalytic hydrogen production from water splitting is considered to be an attractive way to solve the global energy and environment crisis.[23–25] To date, various kinds of photocatalysts,[26] such as TiO_2,[27,28] CdS,[29,30] ZnS,[31] bimetallic sulfides,[32] g-C_3N_4,[33] etc., have been explored. Due to the highly negative reduction of photo-excited electrons and the rapid ratio of electron–hole pairs generation, ZnS has been widely used in

[a]Key Laboratory of Eco-chemical Engineering, Taishan Scholar Advantage and Characteristic Discipline Team of Eco Chemical Process and Technology, College of Chemistry and Molecular Engineering, Qingdao University of Science and Technology, Qingdao 266042, P. R. China. E-mail: inorgxiaozhenyu@163.com; iamzqbx@163.com

[b]State Key Laboratory of Structural Chemistry Fujian Institute of Research on the Structure of Mater, Chinese Academy of Sciences, Fuzhou, Fujian 350002, P. R. China

‡ These authors contributed equally to this work.

photocatalytic hydrogen production process.[34] But the solar-to-hydrogen efficiency of ZnS are still relatively low due to its wide band gap (E_g = 3.67 eV), which limits its practical applications.[35] The construction of heterostructure could combine the both advantages of each individual material,[36–38] which have been proved to be an efficient way to solve this issue. For example, due to the band gap of ZnS containing the bottom of the conduction band of ZnO, the constructed ZnO/ZnS heterostructure can dramatically lower the photo-excitation threshold of single species, and enhanced photocatalytic hydrogen production was achieved.[39] Meanwhile, it is also reported the nanosized ZnO/ZnS heterostructure will further improved its photocatalysis active due to the increased accessible reaction sites and light response as well as the narrowed band gap.[40]

Based on these considerations, we used a facile strategy for preparing ZnO/ZnS heterostructure photocatalysts derived from inorganic–organic hybrid material. Firstly, two new inorganic–organic hybrid zinc phosphite, namely, $[Zn(1,2\text{-bimb})_{0.5}(HPO_3)]_n$ (**1**) and $[Zn(1,4\text{-bmimb})_{0.5}(HPO_3)]_n$ (**2**) (1,2-bimb = 1,2-bis(imidazol-1ylmethyl)benzene; 1,4-bmimb = 1,4-bis((2-methyl-1H-imidazol-1yl)methyl)benzene, Scheme 1), have been synthesized hydrothermally, and structurally characterized by single-crystal X-ray diffraction. Compound **1** generates a three-dimensional (3D) pillared-layer structure with a 2-nodal 3,4-connected **3,4T15** topology. While compound **2** exhibits a 2D hybrid zinc phosphite sheet with 3,4-connected **3,4L83** topology network. Then, through an etching process of Na_2S, a series of ZnO/ZnS heterostructure were prepared by different etching temperature. It is observed that the optimized **1-160** (compound **1** derived ZnO/ZnS heterostructure at 160 °C) possesses the highest H_2 evolution rate of 22.6 mmol g^{-1} h^{-1}, which is 14.5 times higher than commercial ZnS samples. We hope this work could inspire growing interest on the fabrication of other high-performance semiconductor materials by taking the advantage of inorganic–organic hybrid materials *via* a facile strategy.

2. Experimental

2.1. Materials and physical measurements

All reagents and solvents were commercially available and used without any further purification. The crystallographic diffraction data of **1** and **2** were collected with an Agilent Technologies Gemini A Ultra diffractometer equipped with graphite-monochromated Mo-Kα radiation at room temperature. The elemental analyses were performed on a PerkinElmer 2400

elemental analyzer. The FT-IR absorption spectra were recorded on a Nicolet Impact 410 FTIR in the range of 4000–400 cm^{-1} using the KBr pellets. Powder X-ray diffraction (PXRD) measurements were performed on a Bruker D8 Advance X-ray diffractometer using Mo-Kα radiation in the ambient environment. To determine the specific surface area, adsorption–desorption of N_2 gas at 77 K measurements were obtained by a Micromeritics ASAP 2000 gas sorption analyzer. The morphology and structure of the prepared samples were examined by electron microscopy (SEM, Zeiss merlin; TEM, FEI Tecnai G2 F20).

### 2.2. Synthesis of $[Zn(1,2\text{-bimb})_{0.5}(HPO_3)]_n$ (1)

A mixture of $Zn(CH_3COO)_2 \cdot 2H_2O$ (21.9 mg, 0.1 mmol), 1,2-bimb (15.4 mg, 0.06 mmol), H_3PO_3 (41 mg, 0.5 mmol), and H_2O (1.0 mL) was sealed in a glass tube with the pH value of 6.0 adjusted with 25% $[N(CH_3)_4] \cdot OH$ (160 µL), which was heated at 120 °C for 3 days and then cooled to room temperature at a rate of 5 °C h^{-1}. Colorless crystals of **1** were obtained and picked out, washed with acetone, then dried in air. Yield: 77%. Anal. calculated for $C_7H_8N_2O_3PZn$ (%): C 31.76, H 3.02, N 10.59. Found: C 31.85, H 3.08, N 10.59. IR (KBr): ν(cm^{-1}) = 3446 (s), 3114 (m), 2976 (w), 2913 (w), 2387 (m), 1630 (w) 1526 (w), 1456 (w), 1408 (w), 1350 (w), 1247 (w), 1095 (s), 1041 (s), 966 (w), 726 (m), 647 (m), 601 (m).

2.3. Synthesis of $[Zn(1,4\text{-bmimb})_{0.5}(HPO_3)]_n$ (2)

A mixture of $Zn(CH_3COO)_2 \cdot 2H_2O$ (21.9 mg, 0.1 mmol), 1,4-bmimb (15.2 mg, 0.06 mmol), H_3PO_3 (41 mg, 0.5 mmol), and 1.0 mL H_2O/CH_3OH (1 : 1, v/v) was sealed in a glass tube with the pH value of 6.0 adjusted with 25% $[N(CH_3)_4] \cdot OH$ (90 µL), which was heated at 120 °C for 3 days and then cooled to room temperature at a rate of 5 °C h^{-1}. Colorless crystals of **2** were obtained and picked out, washed with acetone, then dried in air. Yield: 68%. Anal. calcd for $C_8H_{10}N_2O_3PZn$ (%): C 34.47, H 3.59, N 10.05. Found: C 34.53, H 3.64, N 10.12. IR (KBr): ν(cm^{-1}) = 3449 (s), 3978 (w), 2922 (w), 2850 (w), 2395 (w), 2331 (w) 1630 (m), 1510 (w), 1422 (w), 1095 (m), 1033 (m), 750 (w), 560 (m).

2.4. Synthesis of compound 1 and 2 derived ZnO/ZnS heterostructure

The as-prepared compound **1** (80 mg) was dispersed in 40 mL aqueous solution of Na_2S (400 mg), and then the mixture was stirred for 3 hours at room temperature. The mixture was transferred to a 100 mL reaction vessel and kept at a specific temperature for 10 hours. After cooled to room temperature, the products were collected by centrifuge and washed by H_2O and EtOH several times. For the samples obtained at different reaction temperature (120 °C, 140 °C, 160 °C and 180 °C), were named as **1-120**, **1-140**, **1-160** and **1-180**, respectively. The **2-140**, **2-160** and **2-180** were prepared through the similar process, but replacing the precursor of **1** to **2** with the related reaction temperature.
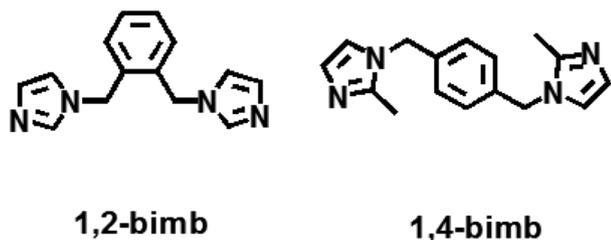
Scheme 1 The structures of organic ligands.

2.5. Evaluation of photocatalytic performance

In a typical process, the as-obtained compounds (10 mg) were dispersed in 100 mL aqueous solution of Na_2S (8.106 g) and Na_2SO_3 (3.151 g). Then, 1 mL K_2PtCl_6 aqueous solution (0.32 mg mL^{-1}) was introduced in the mixture. After stirring 30 min in dark, the suspension was irradiated by a 300 W Xe arc lamp, the hydrogen evolution was evaluated through solar photocatalytic reduction of water, with gas chromatography (GC-7920) equipped with an online thermal conductivity detector (TCD).

3. Result and discussion

3.1. Crystal structure descriptions of compound 1 and 2

Structure of $[Zn(1,2\text{-bimb})_{0.5}(HPO_3)]_n$ (1). Single-crystal X-ray diffraction (SXRD) analysis reveals that compound **1** crystallizes in the orthorhombic system with *Pbcn* space group and shows a 3D pillar-layered structure. As shown in Fig. 1a, **1** contains one Zn^{2+} ion, one HPO_3^{2-} unit, and half of a 1,2-bimb ligand. Each Zn atom is tetrahedrally coordinated by three oxygen atoms from distinct HPO_3^{2-} units and one N atom from 1,2-bimb ligand, showing a distorted tetrahedral coordination. The Zn–O bond-lengths are in the range of 1.910(2)–1.951(2) Å and the Zn–N bond-length is 2.002(3) Å. The O–Zn–O angles are in the range of 103.1(1)–108.5(1)°. Each HPO_3^{2-} unit bonds to three zinc atoms by μ_3-η^1:η^1:η^1 coordination mode with a terminal P–H bond. The P–O distances are in the range of 1.507(2)–1.517(2) Å. As shown in Fig. 1b, the tetrahedral ZnO_3N and HPO_3^{2-} unit are alternately connected to form a wave-like inorganic layer with 4.8^2 topology (Fig. 1c), which are pillared by the linear 1,2-bimb ligand to generate a 3D pillared-layer structure (Fig. 1d). In **1**, the 1,2-bimb ligands are like mirror image arranged between adjacent layers, with a dihedral angles between the imidazole groups and the benzene ring of 75.2(1)°. From a topological view, the 3D network structure can be simplified as a 3D 2-nodal 3,4-connected **3,4T15** topology with point symbol of $\{4.8^2 \cdot 10^3\}$ $\{4.8^2\}$ with Zn and P are viewed as 4-connected and 3-connected nodes, respectively (Fig. S1†).

Structure of $[Zn(1,4\text{-bmimb})_{0.5}(HPO_3)]_n$ (2). Compound **2** crystallizes in the monoclinic system with $P2_1/c$ space group. As shown in Fig. 2a, **2** contains one Zn^{2+} ion, one HPO_3^{2-} unit, and half of a 1,4-bmimb ligand. Each Zn atom is tetrahedrally coordinated by three oxygen atoms from distinct HPO_3^{2-} units and one N atom from 1,4-bmimb ligand, showing a distorted tetrahedral coordination. The Zn–O bond-lengths are in the range of 1.927(2)–1.947(2) Å and the Zn–N bond-length is 2.007(2) Å. The O–Zn–O angles are in the range of 109.8(1)–113.2(8)°. Each HPO_3^{2-} unit bonds to three zinc atoms by μ_3-η^1:η^1:η^1 coordination mode with a terminal P–H bond. The P–O distances are in the range of 1.482(2)–1.539(2) Å. The vertex-shared ZnO_3N and HPO_3^{2-} tetrahedrons are alternately connected to form one-dimensional ladder structure composed of four rings (Fig. 2b), which are further linked by 1,4-bmimb ligands into a 2D hybrid sheet (Fig. 2c). The bis(imidazole) ligand adopts a *trans*-conformation with a dihedral angles between the imidazole groups and the benzene ring of 88.0(9)°. Topologically, the 2D network structure can be simplified as a 3,4-connected **3,4L83** topology with point symbol of $\{4^2 \cdot 6^3 \cdot 8\}$ $\{4^2 \cdot 6\}$ with Zn and P are viewed as 4-connected and 3-connected nodes, respectively (Fig. 2d). It is worth noting that a 3D supramolecular structure of **2** is formed C–H···O hydrogen bonds (Fig. S2†), which originated from hydrogen atoms of 1,4-bmimb ligand and oxygen atoms of HPO_3^{2-} units (C5–H5A···O2 and C4–H4···O1).
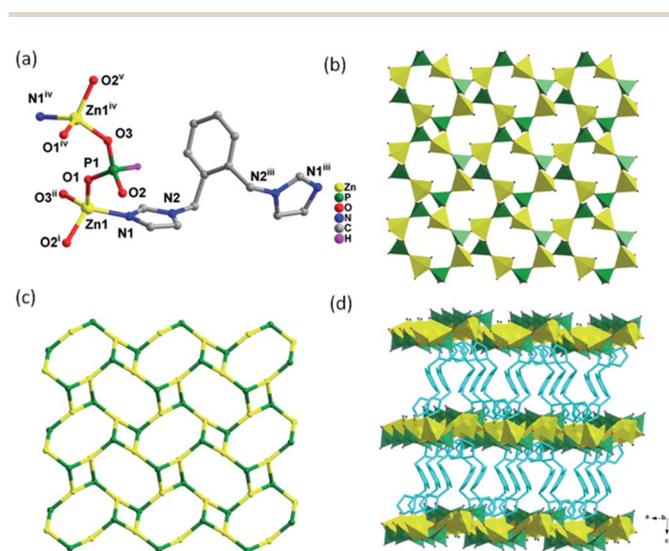
3.2. Structure characterization of 1 and 2 derived ZnO/ZnS heterostructure

For the further application, the phase purity of compound **1** and compound **2** were explored by PXRD tests. As shown in Fig. 3a and b, the experimental patterns are matched well with the stimulated results, and no additional peaks were observed, which demonstrate a high purity for further application. After the Na_2S etching process at 160 °C, the characteristic peaks of **1** and **2** were totally disappeared, as shown in Fig. 3c. Meanwhile, the characteristic peaks at 28.5°, 33.1°, 47.5° and 56.3° belong to the (111), (200), (220) and (311) planes of ZnS (JCPDS: 1-792), and the characteristic diffraction peaks of 31.8°, 34.4° and 36.3° can be indexed to ZnO (JCPDS card: 80-74). The etching process of **1** were also performed at different temperature (120 °C, 140 °C and 180 °C), the obtained products (**1-120**, **1-140** and **1-180**) present similar hybrid composition of ZnO/ZnS, as shown in Fig. 3d.

To explore the porous structure and active surface area, the Nitrogen adsorption–desorption isotherms of **1-120**, **1-140**, **1-160** and **1-180** were tested. It is observed that these curves present a kind of H3-type hysteresis loop with a fast increased N_2 capacity in the range of 0.85–1.00P/P_0, demonstrates a meso/macro-porous structure constructed by nanoparticles.
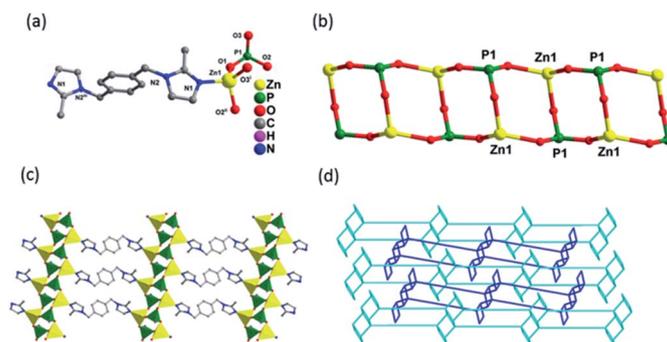

Fig. 1 (a) Coordination environment of the Zn^{2+} in **1** (symmetry code: (i) $1 - x$, $1 - y$, $1 - z$; (ii) $-1/2 + x$, $1/2 - y$, $1 - z$; (iii) $-x$, y, $3/2 - z$; (iv) $1/2 + x$, $1/2 - y$, $1 - z$). (b) Polyhedral representation of the layer structure. (c) The 4.8^2 topology of the layer. (d) Polyhedral representation of 3D structure pillared by 1,2-bimb ligands. For the sake of clarity some hydrogen atoms were omitted (Zn, yellow; C, gray; N, blue; P, green; H, pink).

Fig. 2 (a) Coordination environment of the Zn^{2+} in **2** (symmetry codes: (i) $1 - x$, $1 - y$, $1 - z$; (ii) $-x$, $1 - y$, $1 - z$; (iii) $-x$, $1 - y$, $-z$); (b) ladder structure of **2**; (c) polyhedral representation of the layer structure; (d) the (3,4)-connected **3,4L83** topology. For the sake of clarity some hydrogen atoms were omitted (Zn, yellow; C, gray; N, blue; P, green; H, pink).

According the adsorption–desorption isotherms, the BET surface area of 37.6 m^2 g^{-1}, 48.2 m^2 g^{-1}, 61.5 m^2 g^{-1} and 54.9 m^2 g^{-1} were calculated for **1-120**, **1-140**, **1-160** and **1-180**, respectively. It is observed that **1-160** demonstrates the highest BET surface areas. Furthermore, the meso/macro-porous structure of **1-160** was further confirmed by the Barrett–Joyner–Halenda (BJH) data analysis, as shown in the inset of Fig. 4. Then, the XPS test of **1-160** was perform to confirm the composition ratio of ZnO and ZnS, as shown in Fig. S7.† According to the elements ratio of O : S, the composition ratio of ZnO and ZnS is 1 : 4.2.

To further explore the structure of **1-160**, the SEM (scanning electron microscope) and TEM (transmission electron microscope) were employed. As shown in Fig. 5a and b, it is observed that the block **1** crystal was transfer to a hierarchical structure constructed by a large mounts of small particles. The TEM images demonstrate that each nanoparticles possess clear edge with the size ranged 20 nm (Fig. 5c and d). There are two kinds of lattice fringes with interplanar distances of 0.31 and

0.250 nm can be obtained, which can be matched well with the (100) plane of ZnS and the (101) plane of ZnO, respectively (Fig. 5e), corresponding well with the PXRD results (Fig. 3c). To determine the distribution of Zn, S and O elements, the elemental mappings were also performed. As shown in Fig. 5f, the Zn, S and O elements were evenly distributed in 1–160 particles, implying the formation of ZnS/ZnO hererojunction structure. Those effective ZnS/ZnO hererojunction will benefit for the photocatalytic hydrogen production process.

3.3. Photocatalytic characterization of 1 and 2 derived ZnO/ZnS heterostructure

Photocatalytic hydrogen evolution performances of commercial ZnS, compound **1** and **1** derived ZnO/ZnS at different temperatures, have been investigated. As shown in Fig. 6a, the hydrogen evolution rate of compound **1** derived products are better than compound **1**. With the increasing of sulfuration temperature, hydrogen evolution reaction is gradually
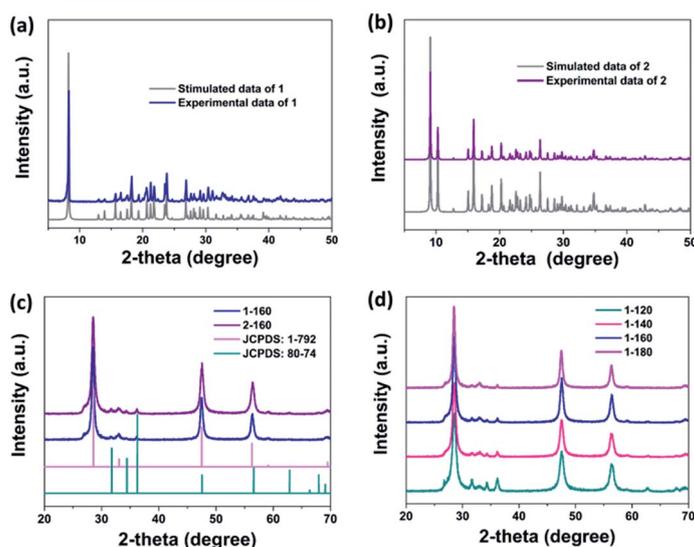

Fig. 3 The XRD patterns of (a) compound **1**, (b) compound **2**, (c) **1-160** and **2-160**, and (d) **1-120**, **1-140**, **1-160** and **1-180**.
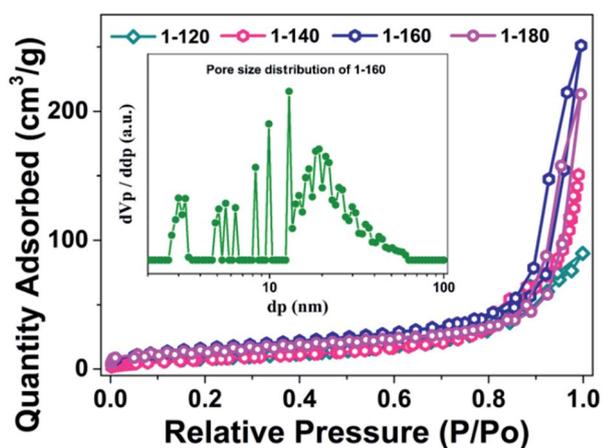
Fig. 4 N$_2$ adsorption–desorption isotherms of **1-120**, **1-140**, **1-160** and **1-180**, inset: the Barrett–Joyner–Halenda (BJH) mesopore size distributions of **1-160**.

enhanced and reaches the highest value for the **1-160**, and then the catalytic efficiency was decreased. The **1-160** displays a photocatalytic hydrogen evolution performances ratio of 22.6 mmol g^{-1} h^{-1}, which is higher than the **2-160** sample of 17.7 mmol g^{-1} h^{-1} (Fig. S4†) and is about tenfold greater than the commercial ZnS. It is also higher than most of other reported ZnS materials, such as ZnS nanoparticles with Ti$_3$C$_2$ MXene nanosheets (502.6 μmol g^{-1} h^{-1}),[41] ZnO/ZnS heteronanostructures-ZnOS-30 (415.3 μmol g^{-1} h^{-1})[39] and ZnS@CdS–Te (592.5 μmol g^{-1} h^{-1}).[42] Meanwhile, to study the photocatalytic stability, **1-160** was estimated under the equal reaction atmosphere for five cycles. As shown in Fig. 6a, an excellent cycle performance of maintaining 87.5% of the initial value was achieved after 25 h irradiation. The band edge positions of the ZnO/ZnS heterostructure was estimated by the equations: $E_{CB} = \chi - E^c - 1/2E_g$. According to the absolute electronegativity and references,[43,44] the values of χ and E_g are

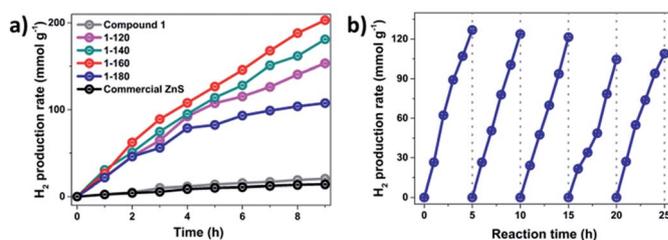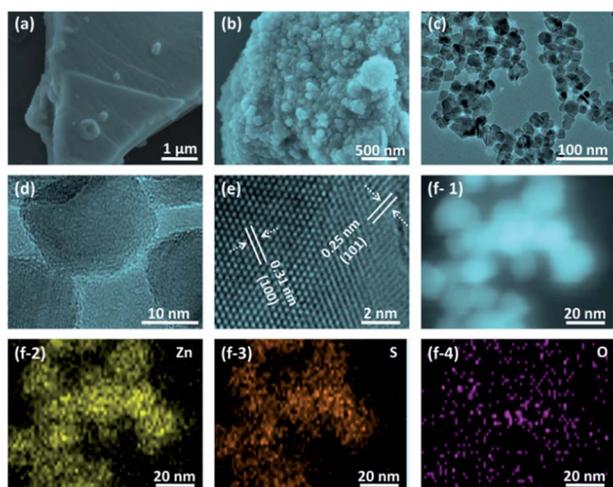**Fig. 5** (a) SEM image of compound **1**, (b) SEM image, (c and d) TEM images, (e) HRTEM image and (f) TEM mapping of **1-160**.

Fig. 6 (a) Plots of photocatalytic H$_2$ evolution amount of **1**, **1-120**, **1-140**, **1-160**, **1-180** and commercial ZnS *vs.* irradiation time. (b) Cycle runs of photocatalytic H$_2$ production over the **1-160** photocatalyst.

5.79 eV and 3.26 eV for ZnO, and 5.26 eV and 3.72 eV for ZnS, respectively. Then, the E_{CB} and E_{VB} were obtained to be −0.34 eV and 2.92 eV for ZnO, and −1.10 eV and 2.62 eV for ZnS. The results demonstrate that the ZnO/ZnS heterostructure can decrease the band gap. Meanwhile, the apparent quantum yield of hydrogen production was calculated to be 12.08% (eqn (S1)†),[45] with a 365 nm bandpass filter.

4. Conclusions

We have successfully synthesized and characterized two novel inorganic–organic hybrid zinc phosphite compound (**1** and **2**) by the self-assembly of the H$_3$PO$_3$ and different bis(imidazole) ligands Zn(II) salts under hydrothermal conditions. Compound **1** displays 3D pillared-layer structure showing a 2-nodal 3,4-connected **3,4T15** topology with point symbol of $\{4.8^2 \cdot 10^3\}\{4.8^2\}$. While compound **2** exhibits a 2D hybrid zinc phosphite sheet with 3,4-connected **3,4L83** topology network, which are further connected by C–H···O and O–H···O hydrogen bonding interactions to form two 3D supramolecular structures. A facile Na$_2$S etching process can be employed to construct a series of ZnO/ZnS heterostructure *via* **1** and **2** as precursors. It is observed that **1-160** demonstrated a very highest H$_2$ evolution rate of 22.6 mmol g^{-1} h^{-1}, exceeding the commercial ZnS samples by more than 14.5 times. This work provides a facile strategy for preparing photocatalysts with efficient photocatalytic hydrogen production derived from inorganic–organic hybrid material, which will inspire growing interest on new ideas for the preparation of other high performance semiconductor materials and structure design.

Conflicts of interest

The authors declare no competing financial interest.

Acknowledgements

References

1 K. Adil, Y. Belmabkhout, R. S. Pillai, A. Cadiau, P. M. Bhatt, A. H. Assen, G. Maurin and M. Eddaoudi, *Chem. Soc. Rev.*, 2017, **46**, 3402–3430.

2 C.-M. Wang, L.-W. Lee, T.-Y. Chang, B.-L. Fan, C.-L. Wang, H.-M. Lin and K.-L. Lu, *Chem.–Eur. J.*, 2016, **22**, 16099–16102.

3 M. L. Ding, R. W. Flaig, H.-L. Jiang and O. M. Yaghi, *Chem. Soc. Rev.*, 2019, **48**, 2783–2828.

4 Y.-B. Huang, J. Liang, X.-S. Wang and R. Cao, *Chem. Soc. Rev.*, 2017, **46**, 126–157.

5 Y. Shi, A.-F. Yang, C.-S. Cao and B. Zhao, *Chem. Rev.*, 2019, **390**, 50–75.

6 Y.-C. Chang and S.-L. Wang, *J. Am. Chem. Soc.*, 2012, **134**, 9848–9851.

7 C.-M. Wang, L.-W. Lee, T.-Y. Chang, Y.-C. Chen, H.-M. Lin, K.-L. Lu and K.-H. Lii, *Chem.–Eur. J.*, 2015, **21**, 1878–1881.

8 L.-M. Li, K. Cheng, F. Wang and J. Zhang, *Inorg. Chem.*, 2013, **52**, 5654–5656.

9 Y.-T. Huang, Y.-L. Lai, C.-H. Lin and S.-L. Wang, *Green Chem.*, 2011, **13**, 2000–2003.

10 M.-J. Sie, C.-H. Lin and S.-L. Wang, *J. Am. Chem. Soc.*, 2016, **138**, 6719–6722.

11 J. B. Wu, C. Y. Tao, Y. Li, Y. Yan, J. Y. Li and J. H. Yu, *Chem. Sci.*, 2014, **5**, 4237–4241.

12 Y.-X. Tan, F. Wang and J. Zhang, *Chem. Soc. Rev.*, 2018, **47**, 2130–2144.

13 A.-Y. Ni, Y. Mu, J. Pan, S.-D. Han, M.-M. Shang and G.-M. Wang, *Chem. Commun.*, 2018, **54**, 3712–3714.

14 M.-L. Han, Y.-P. Duan, D.-S. Li, H.-B. Wang, J. Zhao and Y.-Y. Wang, *Dalton Trans.*, 2014, **43**, 15450–15456.

15 Y. Y. Sun, S. W. Zhao, H. R. Ma, Y. Han, K. Liu and L. Wang, *J. Solid State Chem.*, 2016, **238**, 284–290.

16 Z. Y. Xiao, Y. Y. Sun, Y. X. Bao, Y. X. Sun, R. J. Zhou and L. Wang, *J. Solid State Chem.*, 2019, **269**, 575–579.

17 J. Fan, C. Slebodnick, D. Troya, R. Angel and B. E. Hanson, *Inorg. Chem.*, 2005, **44**, 2719–2727.

18 Y. X. Sun, Y. Y. Sun, H. Zheng, H. L. Wang, Y. Han, Y. Yang and L. Wang, *CrystEngComm*, 2016, **18**, 8664–8671.

19 A.-Y. Ni, Y. Mu, J. Pan, S.-D. Han, J.-H. Li and G.-M. Wang, *J. Mater. Chem. C*, 2018, **6**, 10411–10414.

20 B. K. Tripuramallu, P. Manna and S. K. Das, *CrystEngComm*, 2014, **16**, 4816–4833.

21 J. Zhang, Z. G. Yao, S. J. Liao, J. C. Dai and Z. Y. Fu, *J. Mater. Chem. A*, 2013, **1**, 4945–4948.

22 Z. Y. Xiao, Y. Y. Sun, Y. X. Bao, Y. X. Sun, R. J. Zhou and L. Wang, *J. Solid State Chem.*, 2019, **269**, 575–579.

23 X. Wu, H. B. Zhang, J. C. Dong, M. Qiu, J. T. Kong, Y. F. Zhang, Y. Lia, G. L. Xua, J. Zhang and J. H. Ye, *Nano Energy*, 2018, **45**, 109–117.

24 M. Y. Xing, B. C. Qiu, M. M. Du, Q. H. Zhu, L. Z. Wang and J. L. Zhang, *Adv. Funct. Mater.*, 2017, **27**, 1702624.

25 M. Zheng, Y. Ding, L. Yu, X. Q. Du and Y. K. Zhao, *Adv. Funct. Mater.*, 2017, **27**, 1605846.

26 M. Wang, Y. S. Chang, C. W. Tsao, M. J. Fang, Y. J. Hsu and K. L. Choy, *nanoscale*, 2013, **5**, 363–368.

27 Y. C. Chen, Y. C. Pu and Y. J. Hsu, *Phys. Chem.*, 2012, **116**, 2967–2975.

28 B. Seger, T. Pedersen, A. B. Laursen, P. C. K. Vesborg, O. Hansen and I. Chorkendorff, *J. Am. Chem. Soc.*, 2013, **135**, 1057–1064.

29 C. L. Li, J. Yuan, B. Y. Han and W. F. Shang, *Int. J. Hydrogen Energy*, 2011, **36**, 4271–4279.

30 Y. S. Chang, M. Choi, M. Baek, P. Y. Hsieh, K. Yong and Y. J Hsu, *Appl. Catal., B*, 2018, **225**, 379–385.

31 X. S. Fang, T. Y. Zhai, U. K. Gautam, L. Li, L. M. Wu, Y. S. Bando and D. Golberg, *Prog. Mater. Sci.*, 2011, **56**, 175–287.

32 Q. Li, H. Meng, P. Zhou, Y. Q. Zheng, J. Wang, J. G. Yu and J. R. Gong, *ACS Catal.*, 2013, **3**, 882–889.

33 S. B. Wang, J. L. Lin and X. C. Wang, *Phys. Chem. Chem. Phys.*, 2014, **16**, 14656.

34 K. A. Tsai and Y. J. Hsu, *Appl. Catal., B*, 2015, **164**, 271–278.

35 Y. Chiu, T. Lai, M. Kuo, P. Hsieh and Y. Hsu, *APL Mater.*, 2019, **7**, 80901.

36 P. Y. Hsieh, Y. H. Chiu, T. H. Lai, M. j. Fang, Y. T. Wang and Y. J. Hsu, *ACS Appl. Mater. Interfaces*, 2019, **11**, 3006–3015.

37 M. Y. Chen and Y. J. Hsu, *Nanoscale*, 2013, **5**, 363–368.

38 T. H. Do, C. N. Van, K. A. T. sai, L. T. Quynh and J. W. Chen, *Nano Energy*, 2016, **23**, 153–160.

39 X. X. Zhao, J. R. Feng, J. W. Liu, J. Lu, W. Shi, G. M. Yang, G. C. Wang, P. Y. Feng and P. Cheng, *Adv. Sci.*, 2018, **5**, 1700590.

40 Y. H. Chiu and Y. J. Hsu, *Nano Energy*, 2017, **31**, 286–295.

41 L. Tie, S. Yang, C. Yu, H. Chen, Y. Liu, S. Dong, J. Y. Sun and J. H. Sun, *J. Colloid Interface Sci.*, 2019, **545**, 63–70.

42 Z. C. Xin, L. Li, W. Z. Zhang, T. T. Sui, Y. X. Li and X.-Y. Zhang, *Mol. Catal.*, 2018, **44**, 1–12.

43 Y. F. Lin and Y. J. Hsu, *Appl. Catal., B*, 2013, **130**, 93–98.

44 Y. Li, Q. Ruan, H. Lin, Y. Geng, J. Wang, H. Wang, Y. Yang and L. Wang, *Sci. China Mater.*, 2020, **63**(1), 75–90.

45 H. Lin, B. Sun, H. Wang, Q. Ruan, Y. Geng, Y. Li, J. Wu, W. Wang, J. Liu and X. Wang, *Small*, 2019, **15**, 1804115.